A study on axial and torsional resonant mode matching for a mechanical system with complex nonlinear geometries

Brett Watson, Leslie Yeo, and James Friend[a)]
Department of Mechanical and Aerospace Engineering, MicroNanophysics Research Laboratory, Monash University, Clayton, Victoria 3800, Australia

(Received 2 February 2010; accepted 26 April 2010; published online 4 June 2010)

Making use of mechanical resonance has many benefits for the design of microscale devices. A key to successfully incorporating this phenomenon in the design of a device is to understand how the resonant frequencies of interest are affected by changes to the geometric parameters of the design. For simple geometric shapes, this is quite easy, but for complex nonlinear designs, it becomes significantly more complex. In this paper, two novel modeling techniques are demonstrated to extract the axial and torsional resonant frequencies of a complex nonlinear geometry. The first decomposes the complex geometry into easy to model components, while the second uses scaling techniques combined with the finite element method. Both models overcome problems associated with using current analytical methods as design tools, and enable a full investigation of how changes in the geometric parameters affect the resonant frequencies of interest. The benefit of such models is then demonstrated through their use in the design of a prototype piezoelectric ultrasonic resonant micromotor which has improved performance characteristics over previous prototypes. © *2010 American Institute of Physics.* [doi:10.1063/1.3430537]

I. INTRODUCTION

Mechanical systems designed to operate at a resonant frequency have numerous advantages at small scales. Systems take advantage of the motion associated with resonance to induce motion,[1] enable sensing,[2] and convert motion without the need for gears or joints,[3] resulting in the design of smaller mechanical systems.[4] To successfully make use of such resonant phenomena, it is beneficial to have an insight into how changes in component geometry effect the desired resonant frequencies.[5] For a simple system such as a beam, this may be quite easily determined analytically,[6] but when nonlinearities are introduced, such as a curve to the beam, the analysis quickly becomes complex.[7] The complexity of such models does not allow for an intuitive understanding of how the resonant frequency changes with geometric parameters or the underlying physics of the system.

An alternative to creating these complex mathematical models is to use the finite element method (FEM). The FEM allows the relatively quick determination of the resonant frequencies of a system with complex nonlinear geometries. However, if the system has many parameters or a large parameter range, the computational effort required to optimize the design using this method can be tremendous. Moreover, though we may arrive at our desired design, we will not necessarily understand the effect each geometric parameter has on the outcome. Subsequently, a significant amount of effort is required to determine new optimum parameters even when only slight modifications are made to them.

In this paper, we propose to demonstrate two alternative and simple modeling techniques to gain an understanding of how the geometric parameters of a highly nonlinear geometric system affect its axial and torsional resonant frequencies. The first model makes an approximation of the system by decomposing it into a set of well-understood components. This method gives an analytical approximation of the system, allowing an intuitive understanding of the physics while providing a simple to use design tool. The second, more generalized model uses scaling techniques to enable a rational use of the FEM, which results in a pseudoanalytical approximation of the system. We believe this technique is the first example of the use of general scaling techniques such as nondimensionalization and curve fitting to determine the system stiffness and subsequently the resonant frequencies of a mechanical system. The second model provides less insight into the underlying physics of the system than the first but more easily enables an understanding of the effect of the geometric parameters and provides significantly more insight than the FEM alone. Both techniques may benefit researchers developing complex nonlinear mechanical systems at small scales by reducing design and computational time and providing additional insight to the system characteristics.

The specific test case for this work results from our previous paper[8] where we reported on a piezoelectric ultrasonic micromotor concept that uses coupled axial and torsional displacements of the stator tip to drive the rotor. The axial and torsional coupling was achieved by introducing a set of helical cuts to the cylindrical tube being used as the stator. To improve the micromotor performance, we wish to match the axial and torsional resonant modes of the stator. Doing so will take advantage of the increased stator tip displacements that result from operating simultaneously at both the axial and torsional resonant frequency.

A full analytical solution for such a system would be complex and not intuitive for design, such as the model proposed for a twisted beam.[9] Moreover, a full finite element

[a)]Author to whom correspondence should be addressed. Electronic mail: james.friend@eng.monash.edu.au. URL: http://mnrl.monash.edu.

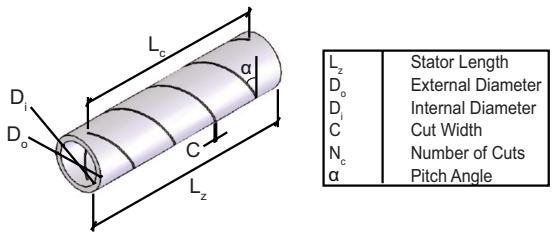

FIG. 1. (Color online) The geometric parameters of the stator that, along with the material properties, describe the system.

parametric analysis of the system geometries would be time and computationally intensive. The two models we demonstrate successfully highlight the relationship of axial-torsional resonant frequencies of the stator to the geometric parameters while being intuitive enough to be used as a design tool. Subsequent fabrication and testing of a micromotor designed using these models demonstrates a significant improvement in performance and provides a way to validate the proposed models.

II. MODELING

A. Stator parameters

1. Nondimensionalization of stator parameters

The stiffness of the stator is a function of the six geometric parameters of the stator design and the material properties

$$K_e = f(D_o, D_i, C, N_c, \alpha, L_c, E, L_z), \tag{1}$$

$$K_r = f(D_o, D_i, C, N_c, \alpha, L_c, G, L_z), \tag{2}$$

where K_e is the axial stiffness and K_r is the torsional stiffness of the stator, E is the Young's modulus, G is the shear modulus, and the geometric parameters are outlined in Fig. 1. The quantity L_c is the cut length which is kept constant at $0.9L_z$ as specified by our design concept, while the density ρ does not affect the stiffness. We can nondimensionalize the system using the Buckingham Pi theorem[10] to arrive at

$$\frac{K_e}{ED_o} = f\left(\frac{D_i}{D_o}, \frac{C}{D_O}, N_c, \alpha, \frac{L_z}{D_o}\right) \rightarrow K_e^* = f(D_i^*, C^*, N_c, \alpha, L_z^*) \tag{3}$$

for the nondimensional axial stiffness and

$$\frac{K_r}{GD_o^3} = f\left(\frac{D_i}{D_o}, \frac{C}{D_O}, N_c, \alpha, \frac{L_z}{D_o}\right) \rightarrow K_r^* = f(D_i^*, C^*, N_c, \alpha, L_z^*) \tag{4}$$

for the nondimensional torsional stiffness.

2. Parameters space of the modeled stator

To validate, compare, and use the models, it will, in part, be necessary to use a model derived using the FEM. For this, we nominate a parameter space that covers a range of geometric values that would be suitable for use in our piezoelectric ultrasonic micromotor.

B. Resonant frequency calculation

Axial and torsional resonant frequencies are calculated for both models in the same way. To determine the harmonic normalized axial resonant frequency, we use

$$\frac{\omega_e}{n} = \frac{1}{2}\sqrt{\frac{K_e}{M}}, \tag{5}$$

where n is the harmonic number, K_e is the axial stiffness as determined from the method under investigation, and M is the mass of the stator, which can be determined using

$$M = \rho D_o\left[\frac{\pi}{4}D_o^2(1 - D_i^{*2})L_z^* - N_c C^* hL\right], \tag{6}$$

where $\rho = 8000\ \mathrm{kg/m^3}$ for 304 stainless steel, h is described by Eq. (16), and L is the total length of the helical cut and can be found using

$$L = [(0.9L_z^* D_o)^2 + (\pi D_o N_r)^2]^{1/2}. \tag{7}$$

For the harmonic normalized torsional resonant frequency, we use

$$\frac{\omega_r}{n} = \frac{1}{2}\sqrt{\frac{K_r}{I_z}}, \tag{8}$$

where K_r is the torsional stiffness as determined from the method under investigation and I_z is the second moment of the area of the stator. To calculate I_z explicitly would be complex; as such, we approximate the second moment of area by ignoring the helical twist and considering an extrusion with a cross-section identical to the stator. This approximation can be calculated using

$$I_z = \frac{\pi}{32}D_o^5 \rho L_z^*\left\{1 - N_c \sin^{-1}\left[\frac{C^*}{\sin(\alpha)}\right]\right\}. \tag{9}$$

Comparisons with data taken from a solid modeling program for a specific stator design show this to be an acceptable approximation with an error of 6.5%.

We can see from this set of equations that the unknown in our system is the stiffness of the stator. It is this that we seek to determine using our models.

C. FEM model

We choose to model the stator stiffness using two models. The first is based on the stiffness of a helical spring, henceforth referred to as the helical spring model (HSM). The second uses scaling techniques to develop a pseudostiffness, referred to as the pseudostiffness model (PSM). For both HSM and the PSM, we require a model using the FEM of the stator with which to compare or make use of.

For this we developed a model using the commercially available software package ANSYS V10.0 (ANSYS Inc., Canonsburg, PA). The stator was modeled using three-dimensional (3D) ten-node tetrahedral structural solid elements, leading to an eigenvalue extraction problem of the form

$$[K]\{\Phi\} = \lambda_i[M]\{\Phi\}, \tag{10}$$

where $[K]$ is the structure stiffness matrix, $\{\Phi\}$ is the eigenvector, λ_i is the eigenvalue, and $[M]$ is the structure mass

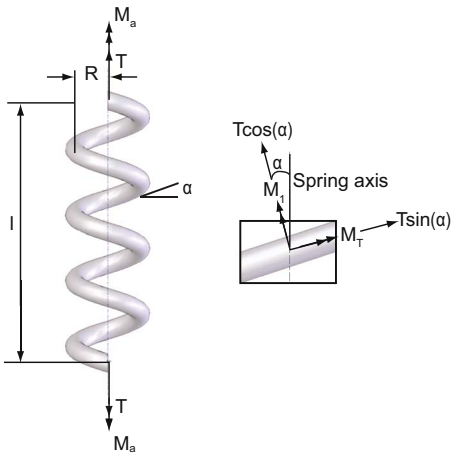

FIG. 2. (Color online) The free-body diagram of the method proposed by Wittrick (Ref. 13) to calculate the equivalent axial and torsional spring stiffness of a helical spring.

matrix. Eigenvalues were extracted using an in-built shifted block Lanczos algorithm based on the theoretical work of Grimes *et al.*[11]

The stator was modeled with free-free boundary conditions. We know that in our system, the mass of the piezoelectric element will be on the order of 500 times larger than that of the stator. In addition, we expect the stiffness of the components to be of the same order. Therefore, it is valid to assume that the resonant frequencies of the two systems would be significantly different; thus, the piezoelectric element would not be coupled with the frequency of the stator. As a consequence of the large difference in resonance frequencies between the piezoelectric element and the stator, the piezoelectric element acts to deliver a harmonic force that parametrically excites the resonance of the stator, while the consequent resonant vibration of the stator has negligible effect on the piezoelectric element's motion. This is the reason for the free-free assumption used here and the close correspondence between FEM-computed and experimentally measured resonance frequencies in Sec. IV B supports this decision. If the proposed modeling methods were to be used for other cases, the boundary conditions for the finite element model would have to be examined in each case.

From the FEM, the first two axial and torsional resonant frequencies were semiautomatically determined using a modified version of the method developed by Friend *et al.*[12] For the third harmonic and higher resonances, the highly nonlinear behavior of the system makes specific mode shapes difficult to determine.

D. HSM

1. Spring stiffness

The seminal equation for the axial and torsional spring stiffness of a helical spring was developed by Wittrick.[13] Using an energy balance and the free-body diagram illustrated in Fig. 2, Wittrick arrived at the expression for the equivalent axial spring stiffness to be

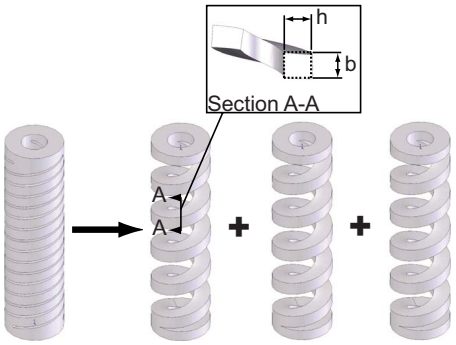

FIG. 3. (Color online) To use the calculation proposed by Wittrick (Ref. 13) to determine the axial and torsional stiffness, the stator is decomposed into a set of helical springs, with the cross-section approximated by a rectangle of dimensions b and h.

$$K_{se} = \frac{\beta_T \cos^2(\alpha) + \beta_1 \sin^2(\alpha)}{LR}, \tag{11}$$

and the equivalent torsional spring stiffness to be

$$K_{sr} = \frac{\beta_1 \cos^2(\alpha) + \beta_T \sin^2(\alpha)}{L}, \tag{12}$$

where β_T is the torsional modulus of the spring cross-section, β_1 is a bending modulus of the spring cross-section, α is the pitch angle of the spring, L is the total length of wire in the spring, and R is the radius of the spring.

Implicit in the derivation of Eqs. (11) and (12) are three assumptions: that the spring cross-section is doubly symmetric, that the spring is wound in such a way that one of the two center lines of every cross-section is normal to the surface of the cylinder of radius R, and that cross-sectional dimensions of the spring are small when compared with the radius of curvature $R \sec^2(\alpha)$ of the helix. The last assumption can be expressed more formally as

$$\gamma^{-2} \ll 1, \tag{13}$$

where γ is defined as

$$\gamma = \frac{R}{k_T} \sec^2 \alpha, \tag{14}$$

in which k_T is the polar radius of gyration of the spring cross-section.

2. Application of Wittrick's stiffness model

To use Wittrick's model to calculate an equivalent stiffness in our model, we decompose the stator into the same number of identical springs as there are number of cuts (N_c). The cross-section of each spring is determined by approximating the remaining tube wall material as a rectangle, as shown in Fig. 3.

Using the nondimensional geometric parameters outlined in Eqs. (3) and (4), we can calculate b and h to be

$$b = \left[\frac{D_o}{N_r N_s \cos(\alpha)}\right]\left\{0.9L_z^* - \left[\frac{C^*}{\cos(\alpha)}\right](N_r N_s + 1)\right\}, \tag{15}$$

$$h = \frac{D_o(1 - D_i^*)}{2}, \tag{16}$$

respectively, in which α can be determined from

$$\alpha = \tan^{-1}\left(\frac{0.9L_z^*}{\pi N_r}\right). \tag{17}$$

Having determined b and h, we can explicitly write expressions for the rest of the variables to determine K_{se} and K_{sr} for one of the system springs,

$$\beta_T = G\left[\frac{bh}{12}(b^2 + h^2)\right], \tag{18}$$

$$\beta_1 = E\left(\frac{bh^3}{12}\right), \tag{19}$$

$$R = \frac{D_o}{4}(1 + D_i^*). \tag{20}$$

We can also write an expression for k_T that will allow us to calculate γ using Eq. (14)

$$k_T = \frac{\sqrt{b^2 + h^2}}{2\sqrt{3}}. \tag{21}$$

The total stiffness of the stator can then be recovered using the parallel spring theorem

$$K_n = N_c \quad K_{sn}, \tag{22}$$

where K is the stiffness of the stator; N_c is the number of cuts; K_s is the stiffness of the spring; when the n subscript is replaced by e throughout, we are referring to the axial resonance; and when r replaces e, we are referring to the torsional resonance. In the above, we have assumed that the small uncut sections of the stator ($0.05L_z$ long at each end) are much stiffer than the equivalent spring stiffness and have ignored these in the stiffness calculation.

E. PSM

1. FEM derived stiffness

To generate a function for the pseudoaxial and the pseudotorsional stiffness and to subsequently determine the associated resonant frequencies, we calculate the stator stiffness from the finite element model using the parameter space outlined in Table I. The stator stiffness is calculated from the FEM using a ratio of the resonant frequency of the stator and the resonant frequency of an uncut tube using Eqs. (5) and (8). This ratio leads to

$$K_{eth} = \left(\frac{\omega_{eth}}{\omega_{et}}\right)^2\left(\frac{M_{th}}{M_t}\right)K_{et} = \omega_e^{*2}M^*K_{et} \tag{23}$$

and

$$K_{rth} = \left(\frac{\omega_{rth}}{\omega_{rt}}\right)^2\left(\frac{I_{zth}}{I_{zt}}\right)K_{rt} = \omega_r^{*2}I_z^*K_{rt}, \tag{24}$$

where K is the stiffness and ω is the resonant frequency, e in the subscript refers to the axial calculation, r refers to the torsional calculation, t refers to the uncut tube, and th refers to the helically cut tube (the stator). M_{th} is the stator mass which can be found using Eq. (6) and I_{zth} is the stator second moment of area which can be found using Eq. (9). K_{at}, K_{rt}, ω_{at}, ω_{rt}, M_t, and I_{zt} can be found using the standard equations for a free-free cylindrical tube.[6] These stiffnesses are then nondimensionalized using Eqs. (3) and (4).

TABLE I. The parameter space used throughout the paper to validate and compare the models under investigation. Note: α is related to N_r by Eq. (17). D_o is the outside diameter, E is the Young's modulus, and G is the shear modulus of a stainless steel 32-gauge tube, the smallest commercially available stainless steel tubing.

Parameter	Low	High	Step size
D_o	0.24 mm	0.24 mm	⋯
D_i^*	0.25	0.75	0.25
L_z^*	2	6	2
C^*	0.04	0.08	0.02
N_r	2	5	1
N_c	2	4	1
E	193 GPa	193 GPa	⋯
G	57.9 GPa	57.9 GPa	⋯

We note there are two inherent assumptions in this analysis. First, that the static stiffness of the uncut tube K_{at} and K_{rt} can be used to find the effective dynamic stiffness of the stator K_{eth} and K_{rth} without introducing a large error. Second, that the difference in mode shape, and thus the effective inertia, of the stator and uncut tube in negligible allow the ratios M_{th}/M_t and I_{zth}/I_{zt} to be used.

2. Pseudostiffness

To generate the pseudostiffness function, we curve-fit the nondimensionalized parameters in Eqs. (3) and (4) against the FEM stiffness derived using Eqs. (23) and (24). We explicitly get

$$K_{nth}^* = f\{D_i^*, C^*, N_c, \alpha, L_z^*\}, \tag{25}$$

where when the n subscript is replaced by e throughout, we are referring to the axial resonance, and when r replaces e, we are referring to the torsional resonance. By fitting a curve to each parameter in turn and improving the least-squares fit toward an ideal of $y=x$ and a coefficient of determination of $R^2=1$, we get the following equations for the pseudostiffness:

$$K_{peth}^* = 0.0135[\cos(D_i^*)^{11.6}](\alpha^{2.5})(L_z^{-1})(N_s^{-1.5})(C^{*-0.58}) \tag{26}$$

and

$$K_{prth}^* = 0.0135[\cos(D_i^*)^{11.684}](\alpha^{1.8})(L_z^{-1})(N_s^{-0.55})(C^{*-0.5}), \tag{27}$$

which can be used to collapse the data, as shown in Fig. 4, where $y=0.9998x$ with $R^2=0.88$ for the axial stiffness and $y=0.9976x$ with $R^2=0.98$ for the torsional stiffness, which demonstrates good agreement with the stiffness calculated using the FEM. We believe the difference in correlation between the axial stiffness $R^2=0.88$ and the torsional stiffness $R^2=0.98$ arises from the assumption in the derivation of the stiffness from the FEM, as defined in Sec. II E 1. Specifi-

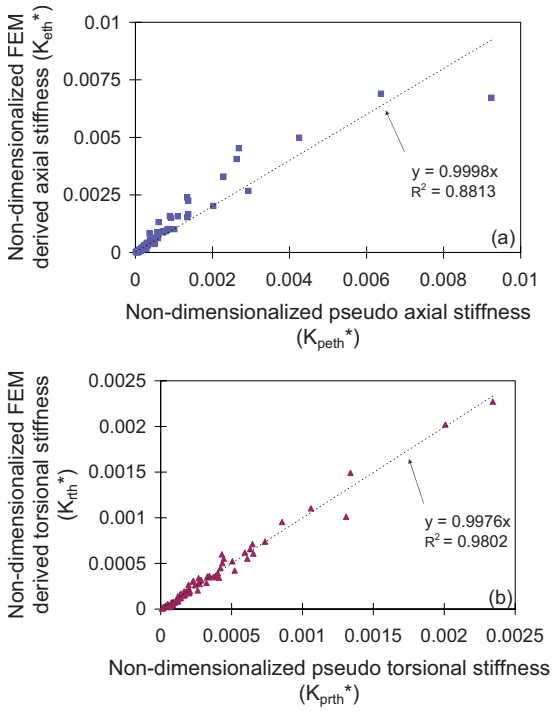

FIG. 4. (Color online) Collapse of (a) the axial pseudostiffness and (b) the torsional pseudostiffness data, using the scaling in Eqs. (26) and (27), respectively, showing good agreement with the stiffness calculated from the FEM.

cally, the effective mass and axial stiffness of the stator is more effected by changes to the geometric parameters than the effective second moment of inertia and torsional stiffness. This is highlighted by limiting $\alpha<0.5$, where the correlation for the axial stiffness improves to $R^2=0.88$ and the correlation for the torsional stiffness decreases slightly to $R^2=0.95$. However, to provide the largest parameter range for design, we do not apply the restriction of $\alpha<0.5$ to the model.

III. MODEL RESULTS AND DISCUSSION

A. Model correlation

We investigate how well the HSM captures the actual characteristics of the geometric system by comparing the HSM-generated resonant frequencies (Secs. II B and II D 2) with resonant frequency data obtained from the finite element model (Sec. II C) over the parameter space outlined in Table I. By performing a linear regression on these sets of data, it is possible to obtain an indication of how well the HSM models the stator. Figure 5 shows a good approximation of the stator's resonant frequencies with a least-squares fit of $y=0.875x$ with a R^2 value of 0.8031.

To examine possible errors in the model, we review the assumptions inherent in Wittrick's spring stiffness model and outlined in Sec. II D 1. From the design, we know that the equivalent springs are "wound" in such a way that one of the two center lines of every cross-section is normal to the surface of the cylinder. For all cases, the maximum γ^{-2} value we find is 0.31, which is acceptable for the assumption $\gamma^{-2} \ll 1$. A ratio of $b/h=1$ indicates a doubly symmetric cross-

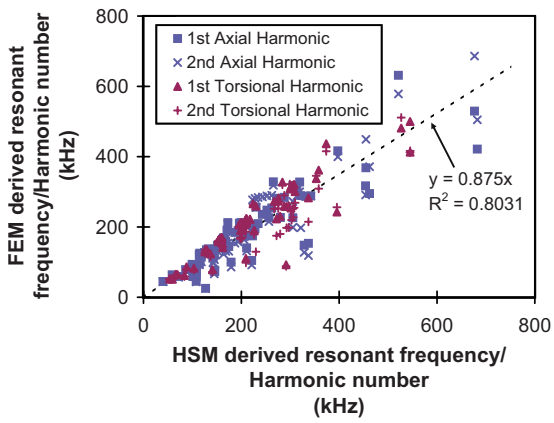

FIG. 5. (Color online) The least-squares fit of the comparison between the HSM and FEM derived resonant frequencies.

section. Calculating the b/h ratio for the parameter space in Table I, we find a minimum of ratio of 0.1 and a maximum of 7.59.

An aspect ratio range of $0.1<b/h<7.59$ is significantly outside the ratio of 1 required by Wittrick's model. To examine the effect of this, we progressively limit the cases that are included in the least-squares analysis to those that have parameters that result in a b/h within certain boundaries. These results are tabulated in Table II.

We find limiting the ranges of aspect ratio in the HSM provides a distinct improvement in the correlation. We also note that there is little change in the effectiveness of the model from a small range $(0.9<b/h<1.1)$ to a range of $0<b/h<2$ or an error of 100%. We find that the parameters that result in a b/h ratio outside of the range $0<b/h<2$ are those that have a thin tube wall (a high D_i^*) and those that have a large pitch angle (α approximately greater than 0.5) while having a low number of cuts ($N_c=2$).

From these results we can determine some important points. First, by using this simplified modeling technique, it is possible to accurately model the resonant frequencies of the system. Second, the simple calculation allows an intuitive understanding of how the physics of the system works. For example, an increase in the pitch angle affects both the

TABLE II. Limiting the parameter cases to ranges of the aspect ratio demonstrates the effect that violating Wittrick's assumption $b/h=1$ has on the HSM accuracy (Ref. 13). Note the number of data points for each least-squares analysis was four times the number of cases signifying two harmonics for two resonant modes.

b/h range	Number of cases	Least-squares fit constant	R^2
All parameter cases 0.1–7.59	72	0.875	0.8031
0.9–1.1	5	0.9676	0.9136
0.75–1.25	20	0.9825	0.8953
0.5–1.5	37	0.9975	0.8859
0.25–1.75	47	1.0034	0.8683
0–2	58	1.0284	0.8819
0–3	65	1.0647	0.8642
0–4	68	1.0755	0.8511

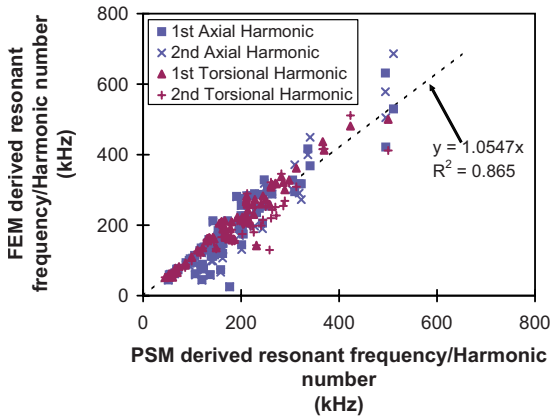

FIG. 6. (Color online) Comparison of the axial and torsional resonant frequencies calculated using the PSM and those obtained using the FEM.

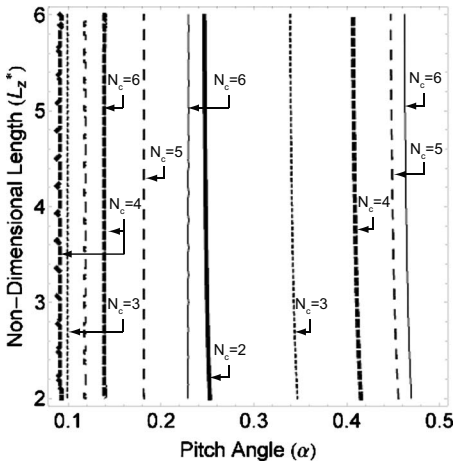

FIG. 7. A typical contour plot of a unity ratio of axial to torsional resonant frequency $\omega_e/\omega_r=1$ against nondimensional length L_z^*, pitch angle α, number of cuts N_c for nondimensional cut width $C^*=0.06$, and nondimensional internal diameter $D_i^*=0.458$.

moment of inertia of the spring cross-section and the applied loading. Last, we find the interesting result that as a design tool, the model for equivalent spring stiffness derived by Wittrick can be applied to a much greater range of problems than the original strict definition of $b/h=1$ suggests.

Using the calculations in Secs. II B and II E to determine the resonant frequencies, the same technique can be used to determine how well the PSM models the system. Figure 6 shows the correlation between the PSM and the FEM is comparable with the best correlation obtained when comparing the HSM and the FEM.

The benefit of the PSM is obvious in two areas. First is the generality of the model. The technique can be used for any single component complex geometrical system without constraints from analytical assumptions. Second, the function quickly shows how important a parameter is to the calculation. This ensures that time is spent most effectively during design. The model is, however, inferior to the HSM in that it does not provide an understanding of the underlying physics of the system and cannot provide information beyond the original task (in this case the calculation of the axial and torsional resonant frequencies).

B. Matching resonant frequencies

For the axial and torsional resonant frequencies to be matched, the ratio must equal 1. From this we write

$$\frac{\omega_e}{\omega_r}=\left(\frac{K_a}{M}\right)\left(\frac{I_z}{K_r}\right)=1. \tag{28}$$

Using Eq. (28) to first examine the HSM, we find that the external diameter D_o has no effect on whether the axial and torsional resonances can be matched. Although more complicated, we also find that the nondimensional length L_z^* plays little part in enabling the matching of axial and torsional resonant frequencies. Figure 7 shows a typical contour plot of $\omega_e/\omega_r=1$ against the stator length L_z^*, pitch angle α, and number of cuts N_c. We see that for any combination of α and N_c that achieves $\omega_e/\omega_r=1$, making changes in L_z^* has no effect. We also note that for $N_c\geq 3$, it is possible to achieve a ratio of one for more than one value of α. For the solution that uses a small value of α, it can be seen that the model breaks down as the value of equivalent spring breadth b nears zero resulting in the broken lines.

Having noted that D_o and L_z^* play little part in being able to match the axial and torsional resonant frequencies, we now focus on the remaining four geometric parameters C^*, D_i^*, α, and N_s. Figure 8(a) plots how the relationship between the parameters varies to ensure $\omega_e/\omega_r=1$. We see that we have a set of curved shells, with the curve being projected in the α-C^* plane. By plotting only the α-C^* plane for a nominal value of $D_i^*=0.458$, we can more closely examine the projected curves, as shown in Fig. 9(a). What we note is that the curves get shorter and more rounded as the value of N_c increases. This means that for $N_c=2$, only a small change in the pitch angle is required for a large change in the nondimensional cut width to ensure a ratio of one is achieved. This is not the case for the higher cases of N_c where a much larger change in α is required.

In Fig. 10(a), we observe that as N_c gets larger, the change in C^* required for a given change in D_i^* gets smaller. Therefore, for a small number of cuts, the change in the nondimensional cut width required to account for any manufacturing changes to the internal diameter would be much greater than for a larger number of cuts.

Figure 11(a) demonstrates that for low values of N_c, only a small change in α is required to offset any changes in D_i^*. However, as the number of cuts increases, D_i^* becomes more dominant to the point where, for $N_c=6$, the axial and torsional resonant frequencies cannot be matched for a stator with a thick wall.

Carrying out the same investigation using the PSM, we find that we can more clearly determine that the outside diameter D_o and the length L_z can be ignored when matching the axial and torsional resonant frequencies. Comparing the results for the HSM and the PSM in Figs. 8(a) and 8(b) shows that, in general, both models produce the same trends, with a set of shells curved in the α-C^* plane.

The two models have some key differences in the changes in relationship necessary to maintain an axial-torsional frequency ratio of one. In Fig. 10, we note that the

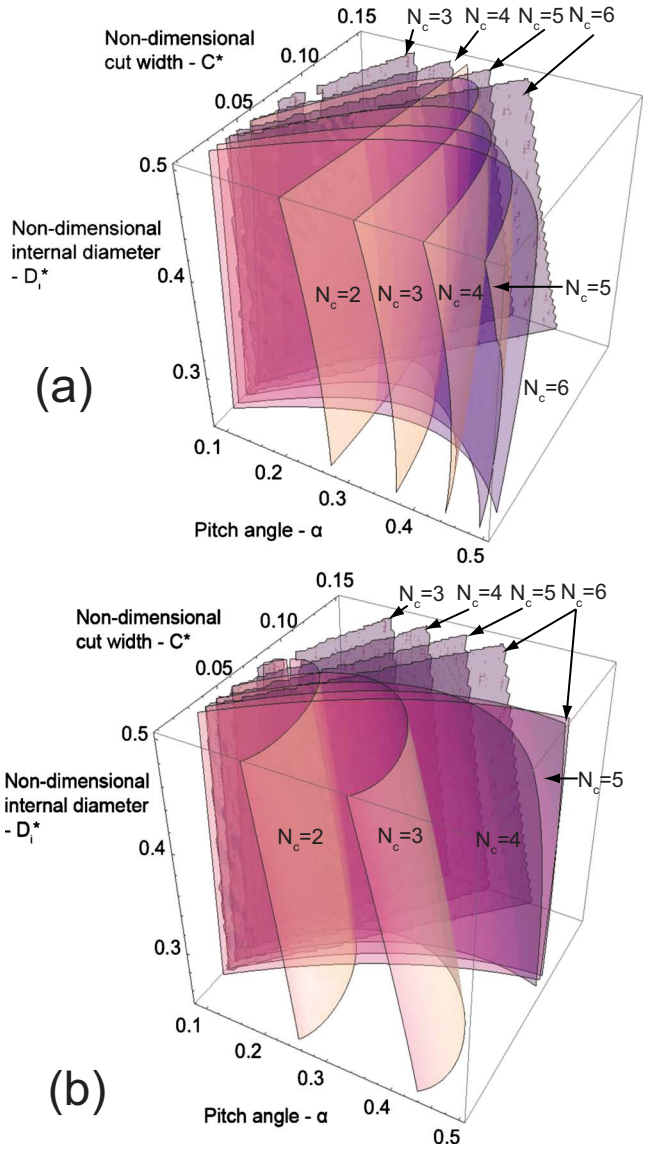

FIG. 8. (Color online) 3D contour plot demonstrating the relationship between the pitch angle, the number of cuts, the nondimensional cut width, and the nondimensional internal diameter to ensure a unity ratio of axial to torsional resonant frequency $\omega_e/\omega_r=1$ for (a) the HSM and (b) the PSM. A nominal value of $L_z^*=3.8$ has been used for the calculation; colors are for visualization only.

PSM predicts that a larger cut width is required for a given internal diameter than the HSM. Also, the path for $N_c=2$ line is significantly different between the two models, which could arise from the error in the HSM when $b/h \gg 1$. The error in the HSM for aspect ratios significantly different from one may also explain the differences we see in the higher numbered cut lines in Figs. 11(a) and 11(b). From Fig. 11(b), we also note that the pitch angle is a much more dominant factor in the PSM than the HSM, while Fig. 9 shows an opposite effect, with the pitch angle being less important in the α-C^* relationship for the PSM than for the HSM. In summary, we note for an intermediate number of cuts ($N_c=3-5$), the two models produce similar trends on how we can match the axial and torsional resonant frequencies.

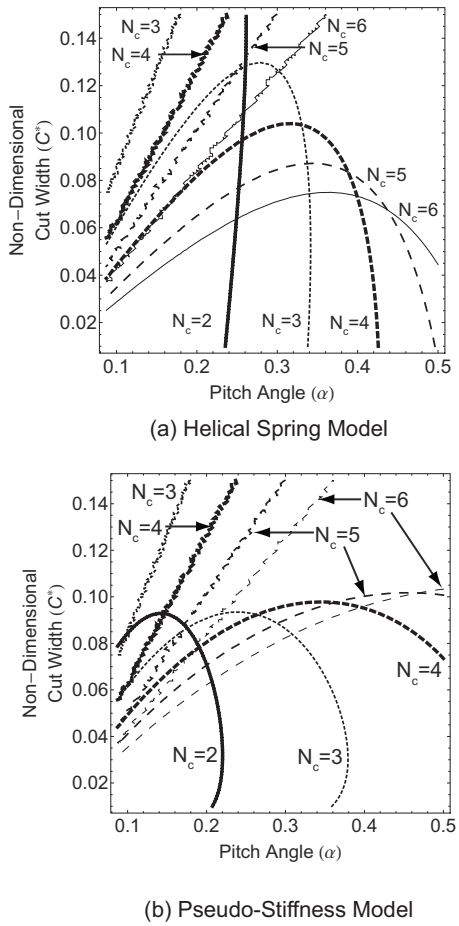

FIG. 9. Parametric relationship for the pitch angle α, the nondimensional cut width C^*, number of cuts N_c for a nondimensional internal diameter of $D_i^*=0.458$, and a nondimensional stator length $L_z^*=3.8$ for (a) the HSM and (b) the PSM.

IV. PROTOTYPE MICROMOTOR

A. Micromotor parameters

The piezoelectric ultrasonic prototype micromotor setup is shown in Fig. 12. The micromotor uses a large piezoelectric element to excite the matched axial and torsional resonant modes in the stator, creating the desired motion in the rotor.[3] The parameters for the stator we have available for testing are listed in Table III. The stator tube is made from 32-gauge 304 stainless steel.

B. Finite element model validation

Both the HSM and the PSM have been shown to produce axial and torsional resonant frequencies that correlate well with a finite element model. To validate the finite element model, we compare axial, torsional, and bending resonant frequencies of Stator 1 calculated by FEM with resonances measured using a laser Doppler vibrometer (LDV) (MSA-400, Polytec GmbH, Waldbronn, Germany). The motor used for the measurements was as outlined in Sec. IV A, with the rotor removed to enable measurement at the required points on the stator tip.

To capture the resonant frequencies, we record the out-of-plane displacement spectra for six points on the stator tip, with the measurement positions shown in Fig. 13(b) resulting

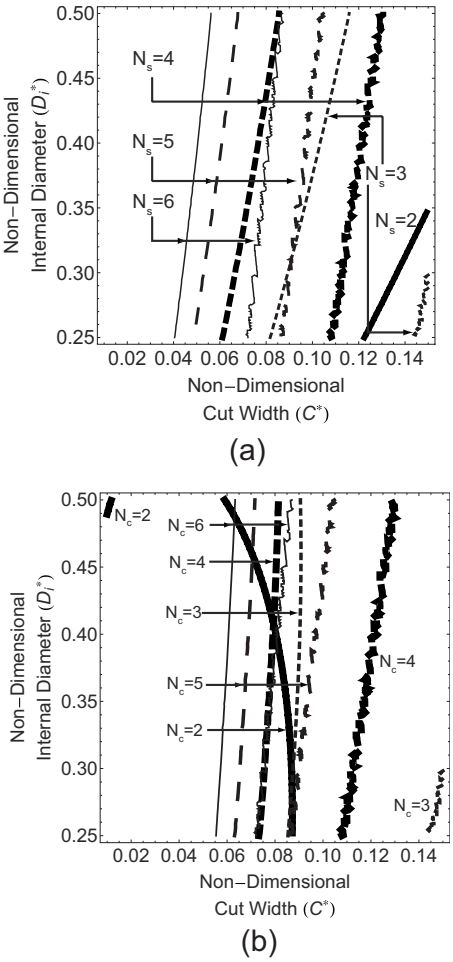

FIG. 10. Parametric relationship for the nondimensional internal diameter D_i^*, cut width C^*, number of cuts N_c for a pitch angle of α=0.2, and a nondimensional cut length of L_z^*=3.8 for (a) the HSM and (b) the PSM.

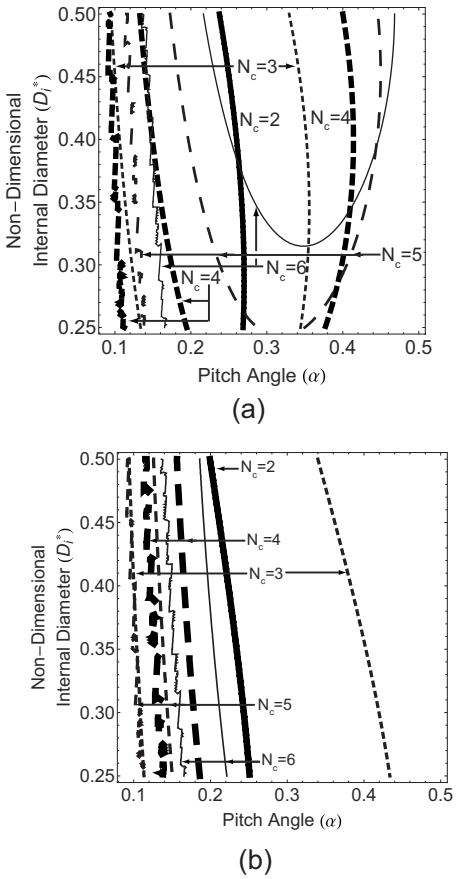

FIG. 11. Parametric relationship for the nondimensional internal diameter D_i^*, the pitch angle α, the number of cuts N_c for a nondimensional cut width C^*=0.06, and a nondimensional length L_z^*=3.8 for (a) the HSM and (b) the PSM.

in the spectra shown in Fig. 13(a). We then use the method outlined by Friend *et al.*[12] to characterize and record the resonant frequencies, which are shown in Fig. 13(a). These measurements demonstrate an average error of less than 10% between the FEM and the measured resonant frequencies, thus validating the FEM model.

C. Micromotor performance

To test the micromotor performance, we use Stator 2 as outlined in Table III. Using a signal generator and amplifier (Rohde & Schwarz-SML 01 and NF-HSA 4501, North Ryde, New South Wales, Australia), the PZT element was driven at each of the trial frequencies, which included each of the finite element model derived axial and torsional resonant frequencies using a bandwidth of ±5% to allow for manufacturing tolerances.

The micromotor demonstrated bidirectional operation with clockwise rotation at the third harmonic (732 kHz) and counterclockwise rotation at the second harmonic (526 kHz). Micromotor performance was determined using the method by Nakamura *et al.*[14] Rotor motion was recorded using a laser Doppler velocimeter (Canon LV-20Z, Utsunomiya, Japan). A maximum clockwise angular velocity of 830 rad/s (7925 rpm) was recorded at an input of 20 V_{p-p} and 732 kHz. Based on the curve in Fig. 14, the average clockwise start-up torque was 47 nNm with a peak of 51 nNm and a minimum of 39.8 nNm. The average braking torque was calculated to be 17.8 nNm. A maximum counterclockwise angular velocity of 1600 rad/s (15 280 rpm) at 32.1 V_{p-p} and 526 kHz was recorded.

As a measure of the improvement in performance possible through the matching of axial and torsional resonant modes, the current test micromotor shows an increase in angular velocity of a minimum of 5.5 times across all runs

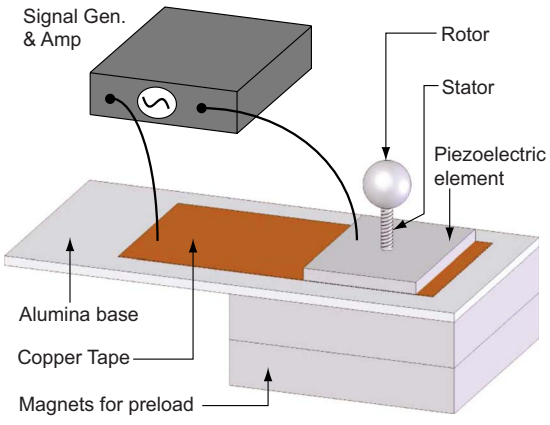

FIG. 12. (Color online) Schematic showing the test setup for the piezoelectric ultrasonic micromotor.

TABLE III. Parameters for the available test stators.

Parameter	Stator 1	Stator 2
Outside diameter (D_o)	241 μm	241 μm
Nondimensional inside diameter (D_i^*)	0.458	0.458
Nondimensional length (L_z)	3.8	3.8
Nondimensional cut width (C^*)	0.04	0.04
Pitch angle (α)	0.214	0.302
Number of cuts (N_c)	2	3
Frequency ratio (ω_e/ω_r) from HSM	0.86	0.91
Frequency ratio (ω_e/ω_r) from PSM	0.88	0.99

when compared with our original micromotor that did not have matched axial and torsional resonant frequencies.[8] In addition to angular velocity, the start-up torque increased by a minimum of three times. During the performance measurement in both micromotors, the preload was modified to ensure that maximum performance was achieved.

V. CONCLUSIONS

We have demonstrated the use of two simple, novel modeling techniques to examine the effect of changes in geometric parameters on the axial and torsional resonant frequencies of a complex nonlinear system. The first model, the HSM, decomposes the system into simpler, well-understood components giving an accurate analytical model of the system. The second model, the PSM, uses scaling techniques to produce a model that reduces computational time and improves insight into the system when compared with the use of the FEM alone. The pseudostiffness technique in particular shows great potential as a generalized tool for the analysis and design of a multitude of complex nonlinear mechanical systems. Due to the simplicity of the methodology, almost any system that can be accurately modeled using a FEM could be analyzed with the PSM. The methodology could be applied to other systems where the resonant vibration is important such as other ultrasonic motor designs, microcantilever beam designs, or possibly other classes of motors such as electrostatic. Moreover, the methodology may be used to investigate other parameters, such as the output force or tip displacement of thermal actuators.

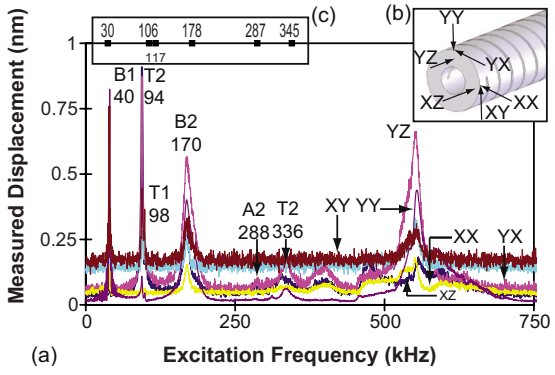

FIG. 13. (Color online) Comparison of stator resonant frequencies obtained from (a) LDV-recorded out-of-plane displacement spectra, using the measurement positions detailed in (b), and (c) finite element model-calculated frequencies for the stator detailed in Stator 1 of Table III.

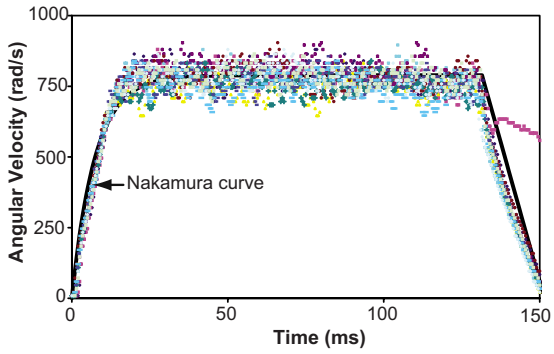

FIG. 14. (Color online) Angular velocity as a function of time, for a test micromotor with closely matched axial and torsional resonant frequencies. A step voltage of 20 V_{p-p} and an operating frequency of 732 kHz was used. The fitted curve is derived from the method by Nakamura *et al.* (Ref. 14) and is the average obtained across all runs.

Using the two models for a specific test case of a piezoelectric ultrasonic micromotor with helical stator geometries, we were able to map the parametric relationships that ensure all axial and torsional modes are matched. This exercise demonstrated that the outside diameter and stator length were unimportant when trying to match axial and torsional resonant frequencies, whereas strong dependence on the cut width and pitch angle were observed.

We demonstrated that a prototype micromotor with closely matched resonant frequencies had a significant improvement in performance over an existing prototype upon applying this knowledge.

ACKNOWLEDGMENTS

This work was made possible in part by Grant Nos. SM/07/1616 and SM/06/1208 from the CASS Foundation, Grant No. DP0773221 from the Australian Research Council, and the New Staff and Small Grant Scheme funds from Monash University. This work was performed in part at the Macquarie/ATP node of the Australian National Fabrication Facility, a company established under the National Collaborative Research Infrastructure Strategy to provide nanofabrication and microfabrication facilities for Australia's researchers.

[1] C. J. Morris and F. K. Forster, J. Microelectromech. Syst. **12**, 325 (2003).
[2] K. M. Hansen and T. Thundat, Methods **37**, 57 (2005).
[3] B. Watson, J. Friend, and L. Yeo, Sens. Actuators, A **152**, 219 (2009).
[4] J. Friend, L. Yeo, and M. Hogg, Appl. Phys. Lett. **92**, 014107 (2008).
[5] S. Subramanian and N. Gupta, J. Phys. D: Appl. Phys. **42**, 185501 (2009).
[6] S. S. Rao, *Mechanical Vibrations* (Addison-Wesley, Reading, 1995).
[7] B. Kang, C. H. Riedel, and C. A. Tan, J. Sound Vib. **260**, 19 (2003).
[8] B. Watson, J. Friend, and L. Yeo, J. Micromech. Microeng. **19**, 022001 (2009).
[9] K.-C. Liu, J. Friend, and L. Yeo, J. Sound Vib. **321**, 115 (2009).
[10] B. R. Munson, D. F. Young, and T. H. Okiishi, *Fundamentals of Fluid Mechanics* (Wiley, New York, 1998).
[11] R. G. Grimes, J. G. Lewis, and H. D. Simon, SIAM J. Matrix Anal. Appl. **15**, 228 (1994).
[12] J. Friend, K. Nakamura, and S. Ueha, IEEE Trans. Ultrason. Ferroelectr. Freq. Control **51**, 870 (2004).
[13] W. H. Wittrick, Int. J. Mech. Sci. **8**, 25 (1966).
[14] K. Nakamura, M. Kurosawa, H. Kurebayashi, and S. Ueha, IEEE Trans. Ultrason. Ferroelectr. Freq. Control **38**, 481 (1991).